*Q. J. R. Meteorol. Soc.* (1995), **121**, pp. 1323–1348

# Comparison between the orographic response of the ECMWF model and the PYREX 1990 data

By FRANÇOIS LOTT*

*European Centre for Medium-range Weather Forecasts, UK*

(Received 17 May 1994; revised 6 October 1994)

SUMMARY

Recent observations and analyses of the atmospheric flow in the vicinity of the Pyrénées made during PYREX are compared with numerical experiments carried out with the T213L31 European Centre for Medium-range Weather Forecasts (ECMWF) global model. This study shows that the model simulates a certain proportion of the measured pressure drag, but always underestimates it. In the current model, this deficit is not adequately made up by any of the parametrized subgrid-scale processes. When the flow is along the range, the pressure-drag value depends on the synoptic background flow structure. It is close to zero when the flow impinging on the range is baroclinic. It is not zero when the atmosphere is more barotropic (e.g. in the absence of any fronts) and the model misses important lift processes. When the flow is normal to the ridge, the model response to the mountain forcing is essentially ageostrophic. In this case comparison between the vertical profiles of the model stresses and the measured profile suggests that further drag should be applied in the model at low level. This is supported by comparisons of isentropic diagnostics, from the ECMWF model and the French mesoscale model, Peridot. These diagnostics show that the ECMWF model underestimates irreversible low-level processes, such as the flow separation on the mountain flanks and the associated downstream wake, which can be related to the drag. They also show that low-level parametrized drags have a realistic impact on the model simulation of the mountain wake. This analysis supports the current developments at the ECMWF of a new subgrid-scale orographic drag scheme which parametrizes the low-level impact of mesoscale mountains.

KEYWORDS: Isentropic diagnostics Gravity waves Mountain flow Pressure drag Parametrization Pyrénées

## 1. INTRODUCTION

In most studies concerned with the representation of orography in numerical weather-prediction models and general-circulation models, attention has been focused either on the parametrization of subgrid-scale mountains or on the proper representation of the planetary-scale massifs. The first approach has led to the introduction of the gravity-wave drag schemes (Boer *et al.* 1984; Palmer *et al.* 1986). The second has proved that the use of an envelope orography, for example, improves the representation of the large-scale planetary waves (Wallace *et al.* 1983). Both approaches have led to significant decreases of the systematic errors of forecasting systems. With increasing computer power and the associated improvements in model resolution, this distinction between resolved and unresolved motions becomes more and more problematic. For instance, many examples show that since the introduction of the T213 forecasting system at the European Centre for Medium-range Weather Forecasts (ECMWF), the model can have an ageostrophic response near mountains, characterized by long gravity waves and strong föhn. This then raises two important questions: does the model properly reproduce part of the mesoscale dynamics? If it does, is there a need to enhance the impact of the mountain on the flow by some subgrid-scale parametrization scheme? The PYREX program (Bougeault *et al.* 1993) provides a coherent database from which to approach these questions for the case of the Pyrénées massif (Fig. 1).

In the present paper, the representation of the mesoscale mountain dynamics in the ECMWF model is compared with direct field measurements of quantities such as the pressure drag, measured along a fixed meridional transect of the Pyrénées (Bougeault *et al.* 1993), hereafter referenced as the PYREX transect. The present study is based on the

* Present affiliation: Laboratoire de Météorologie Dynamique du CNRS, Ecole Normale Supérieure, 24 rue Lhomond, 75231 Paris Cedex 05, France.

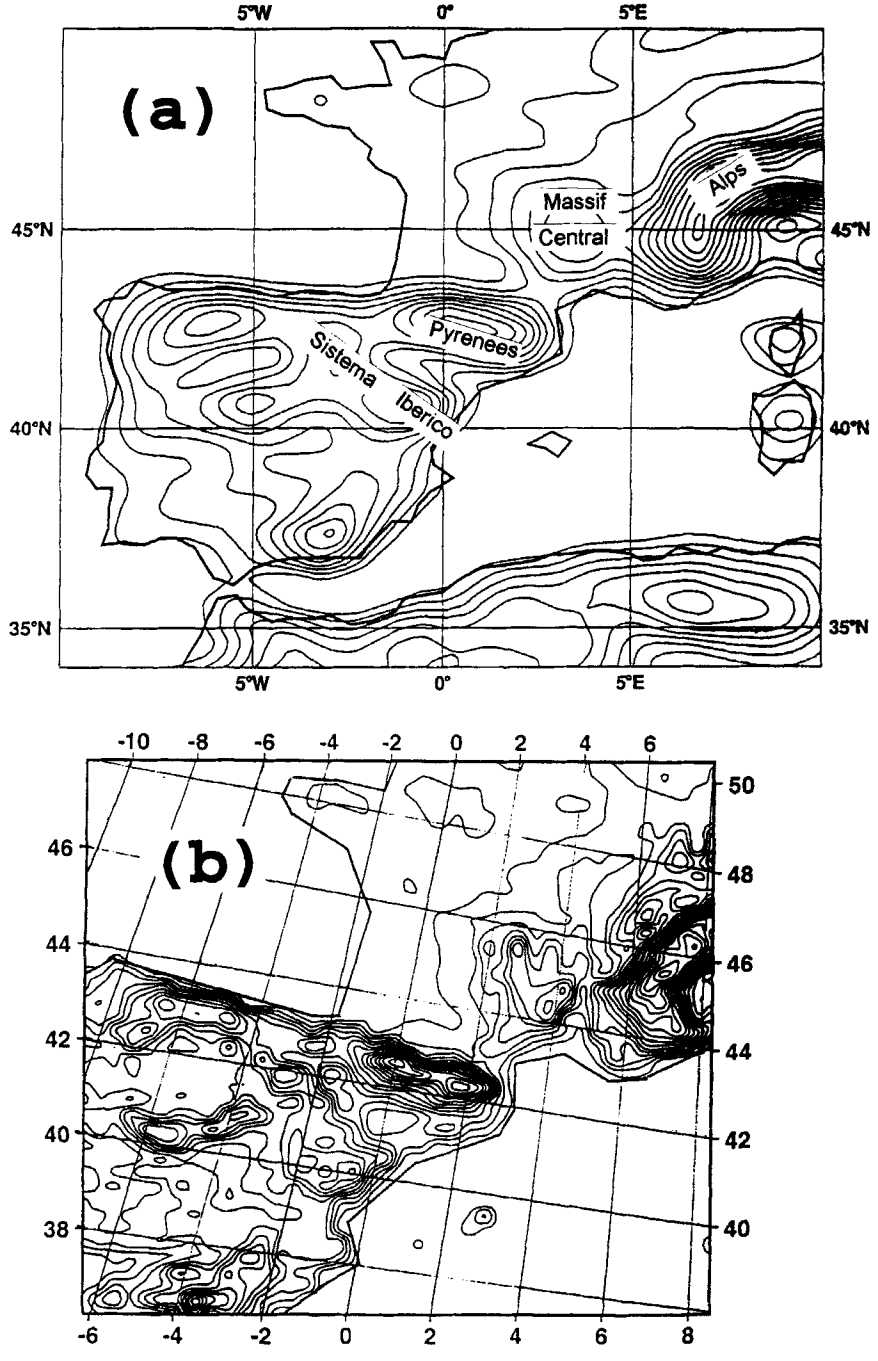


Figure 1. Model orography over south-western Europe for (a) the ECMWF model and (b) the Peridot model. Contour interval = 200 m.

ECMWF re-analysis of the PYREX data, which covers the two months of the experiment. It includes a very large range of incident-flow configurations. For example, the along-ridge (nearly zonal) cases, which are not often studied in the literature (Thorpe *et al.* 1993), show a rather surprising behaviour regarding the pressure drag. For these, the pressure-drag vector has a component perpendicular to the incident flow, which can be very different to the 'lift' force exerted on mountains and due to the background synoptic pressure gradient (Smith 1979a). There has been much more work that considers flow oriented perpendicular to the ridge and flow over small-scale isolated obstacles. Typically, these configurations correspond to most of the PYREX periods of intense observation (POIs), and particularly to POI3 (18 UTC 14 October 1990–12 UTC 15 October 1990) and POI9 (06 UTC 14 November 1990–12 UTC 16 November 1990), during which surface-drag measurements were complemented by aircraft measurements of the vertical profiles of the momentum fluxes above the PYREX transect. As during previous campaigns (see, for instance, Hoinka (1985) for the Alps), it was found (Bougeault *et al.* 1993) that the amplitude of the pressure drag is significantly larger than the amplitude of the measured momentum fluxes. In the present work, it will be verified that a similar discrepancy occurs in the ECMWF model. These suggest that the retardation of the flow by the mountain occurs mainly at low level. To understand more fully how the retardation effect of the mountain is felt by the atmosphere at larger scales, these direct and rather local comparisons are complemented by isentropic diagnostics of the flow dynamics. These diagnostics allow us to detect directly the low-level irreversible processes, which can be related to the mountain drag. They show that significant energy dissipation (observed on Bernoulli function maps) and wake formation mainly occur at low level in the model. To estimate whether the ECMWF model properly represents these low-level flow patterns, the isentropic diagnostics of the ECMWF model are compared with similar analyses done with the French limited-area model, Peridot.

Section 2 briefly describes the data and the analyses. Section 3 discusses the amplitudes of the different drags exerted by the mountain on the model flow, and compares them with the pressure drag measured along the central transect during PYREX. The model pressure drag is then interpreted using two predictors. One is related to the Coriolis drag (or lift drag) concept, mostly relevant during the along-ridge cases. The other is related to the gravity waves controlling the ageostrophic dynamics around the mountain, relevant when the flow is perpendicular to the ridge. This is followed by a comparison between the measured momentum-flux profiles and those diagnosed from the model during normal-ridge configurations. The model dynamics for two along-ridge cases are discussed in section 4. In section 5 a description of the flow dynamics on isentropic surfaces is given in two normal-ridge cases. Also in section 5, the model results are discussed and compared with similar diagnostics of the Peridot model.

## 2. Presentation of the model data

Details of the PYREX field program can be found in Bougeault *et al.* (1993). Details of the Peridot analyses during PYREX (these are provided with the database every six hours during the PYREX POIs, covering approximately 25% of the two months of the experiment) can be found in Bougeault and Mercusot (1992). Briefly, it is a standard optimal interpolation analysis done with the French mesoscale forecasting system Peridot. The number of radiosoundings have been tripled around the Pyrénées to include the extra radiosondes launched close to the Pyrénées during the PYREX's PIOs. Satellites and surface observations have been doubled, using a 6-hour assimilation step instead of the operational 12-hour assimilation step. The horizontal resolution is close to 30 km, and this analysis is mainly suitable for diagnosis of the low-level flow since higher levels of the

troposphere are poorly represented: the altitudes of the last three highest levels are 8 km, 12 km and 18 km respectively.

The ECMWF re-analysis of the PYREX data has been done with the T213L31 optimal interpolation schemes, operational at the Centre during autumn 1992. It covered the 2 months of the experiment and was archived every 6 hours. It uses all the conventional WMO data available during the PYREX period, plus the extra radiosoundings made during the PIOs. Throughout this paper, this analysis, as well as short-range forecasts, are used to describe the ECMWF model dynamics around the mountain.

## 3. General discussion on the different model mountain drags

During the PYREX campaign (Bougeault *et al.* 1993) particular attention was paid to the measurement of the pressure drag at the surface and the vertical profiles of the momentum flux. In the following the question of whether or not these measured quantities are being reproduced in the model, either explicitly or through parametrized subgrid-scale processes, will be investigated. When the central transect goes from the foot of the Spanish Pyrénées (arbitrary located at $y = 0$) to the foot of the French massif (located at $y = L$), the surface drag per unit length may be expressed as:

$$-\int_0^L P_s \frac{\partial h}{\partial y}\frac{dy}{L} + \int_0^L (\tau_{GW} + \tau_{BL})(P_s)\frac{dy}{L} \tag{1}$$

where $P_s$ is the surface pressure and $h(y)$ the mountain profile along the central transect. To follow the model convention, the total drag (1) has been split into three parts: the first term in (1) corresponds to the explicit model pressure drag, the second and third terms correspond to the subgrid-scale parametrized gravity-wave (GW) surface stress and to the boundary-layer (BL) surface stress. Similarly, the total momentum flux at a given pressure level $P$ is:

$$\int_0^L \left(-\frac{\omega v}{g} + \tau_{GW} + \tau_{BL}\right)(P)\frac{dy}{L} \tag{2}$$

where $v$, $\omega$ and $g$ are the meridional wind, the pressure tendency and the acceleration due to gravity, respectively. The first term in (2) corresponds to the vertical flux of meridional momentum explicitly resolved by the model. The second and the third terms in (2) correspond to the parametrized gravity-wave stress and boundary-layer stress, respectively. As far as possible, the meridional path along which these integrals are calculated in the model is close to the PYREX transect.

At this stage of the discussion, it is useful to recall briefly how the gravity-wave and the boundary-layer parametrization schemes work. The gravity-wave drag scheme is a modified version of the one proposed by Palmer *et al.* (1986). The surface gravity-wave drag is given by,

$$\tau_{GW}(P_s) = \tfrac{1}{2} k \rho_s U_1 N_1 H^2 \tag{3}$$

where $k = 2.5 \times 10^{-5}\text{m}^{-1}$ is a constant characterizing the horizontal wavelength of the subgrid-scale mountain, $\rho_s$, $U_1$, $N_1$ and $H^2$ are the atmosphere density at the ground, a low-level incident wind, a low-level buoyancy frequency, and the subgrid-scale orographic variance calculated with the US Navy ($10' \times 10'$) orography data set. Taking account of Palmer *et al.* (1986), the gravity-wave drag amplitude has been modified to introduce directional flow effects by calculating the orographic variance in the direction of the low-level flow (Miller *et al.* 1989). This drag is redistributed in the vertical at levels where the

gravity waves are unstable or below a critical level. Following the work of Miller *et al.* (1989), this part of the scheme has also been modified to represent low-level drag effects related to trapped lee waves. Seventy per cent of the surface drag is returned uniformly over the lowest 1500 m of the model. A parametrization of nonlinear wave-drag effects (Peltier and Clark 1983) has also been introduced. It did not appear to be significantly active in the model over the Pyrénées. At the time for which the ECMWF re-assimilation of the PYREX data was done, the boundary-layer scheme followed that proposed by Louis (1979), in which the surface-flux parametrization is based on Monin and Obukhov (1954) similarity theory, and the eddy flux coefficients above the surface are expressed as a function of the bulk Richardson number (Louis 1979). The surface scheme is described by Blondin (1991). In the boundary-layer scheme, the impact of mountains is introduced by making the roughness length proportional to the subgrid-scale mountain standard deviation times the slope, both quantities being estimated from the US Navy data set (Tibaldi and Geleyn 1981). Over the Pyrénées, this gives a roughness length which is of the order of 10 m. The fact that the parametrized boundary-layer drag is introduced in the comparison between the model mountain drag and the measured pressure drag is not strictly licit. In fact, the microbarographs along the PYREX transect are spaced by typically 10 km, and cannot capture the pressure drag related to smaller-scale features. Nevertheless, there are many uncertainties regarding the turbulent stress value, when a stably stratified flow impinges a high and sharp 3-dimensional ridge. Furthermore, in models, the boundary-layer drag enhancement above mountains is essentially a convenient way to limit there the amplitude of the low-level flow. In the past (Tibaldi and Geleyn 1981), this parametrization was introduced rather intuitively and has not been validated in detail. Nowadays, progress in the theory of mesoscale flows over mountains show that these low-level flow effects can be related to nonlinear mesoscale features. This point of view is supported by the fact that a certain amount of the pressure drag measured during PYREX is probably related to a retardation of the low-level flow. In this context, the increase of the roughness length over mountains partly parametrizes these mesoscale low-level effects, and the turbulent stress in the model has to be included in the comparison with the measured drag. Then, the total mountain drag in the model has to be at least as large as the measured pressure drag.

### (*a*) *Comparison between modelled and measured pressure drags*

The calculation of the pressure drag measured along the central transect during the campaign (Bougeault *et al.* 1993) and those calculated from the ECMWF analysis and the Peridot analysis follow the formula of Davies and Phillips (1985):

$$D = \frac{1}{L} \int_{z_{\min}}^{z_{\max}} (P_{\mathrm{NORTH}} - P_{\mathrm{SOUTH}})\, \mathrm{d}z \tag{4}$$

where $L$ is the length of the transect, and $P_{\mathrm{NORTH}}$ and $P_{\mathrm{SOUTH}}$ represent the pressure on each side of the mountain at a given height, $z$. They are calculated from the model grid points by a linear interpolation in the vertical. $Z_{\max}$ is the altitude of the highest grid point of the transect and $Z_{\min}$ is the lowest altitude along the transect. In both models the transect was chosen to be as close as possible to the PYREX north–south central transect, the orientation of which is close to the Greenwich meridian. In the ECMWF model, advantage has been taken of the fact that the Greenwich meridian is well represented on the reduced Gaussian grid because the first point of each latitude row is located on it. Five grid points surrounding the mountain top have therefore been chosen on this meridian to define the model transect. In the Peridot analysis the grid used does not have any axis whose orientation is as close to that of the PYREX transect. In the Peridot model, the transect has been defined along

a model axis which passes the summit of the ridge close to longitude 0 (Greenwich), and whose inclination relative to the Greenwich meridian is 16°. The different transects are shown in Fig. 2.

It is noteworthy that the changes in the pressure drag in the ECMWF model (Fig. 3) are well correlated with the measured drag. The maxima, minima and zeros of the model drag always correspond to those of the measured drag. On the other hand, at the peaks, the amplitude of the ECMWF drag is typically half the measured drag. In the Peridot model, the amplitude of the variations in the pressure drag are as large as that of the measured drag. Nevertheless, the Peridot drag has a positive systematic error so that when the drag is negative its amplitude is too small (days 11, 12, 13, 14, 26). This kind of discrepancy is not surprising since the orientation of the Peridot's transect is significantly different from the orientation of the PYREX transect, which forbids a point to point comparison between the Peridot drag and the measured drag.

### (*b*) *Predictors of the ECMWF pressure drag*

Although well correlated with the measured drag, it is plausible that the pressure drag in the ECMWF model is a passive signature of the synoptic pressure gradient, associated with the synoptic weather changes over Europe. In this case, applying geostrophic balance to estimate the synoptic pressure gradient from the upstream wind, the model pressure drag may be proportional to the mountain volume times the along-ridge wind (Smith 1979a). This gives the following lift force per unit length:

$$D_C \approx -\rho_0 h_m U f \tag{5}$$

(hereafter referred to as the Coriolis predictor of the pressure drag). $U$ is the incident flow component along the ridge, $h_m$ is the mean mountain elevation along the ridge, $\rho_0$ is the low-level air density and $f$ is the Coriolis parameter. The model pressure drag can also be related to an effective dynamical response of the atmosphere to the mountain forcing. With a typical meridional length-scale of 100 km, the model response to the mountain forcing

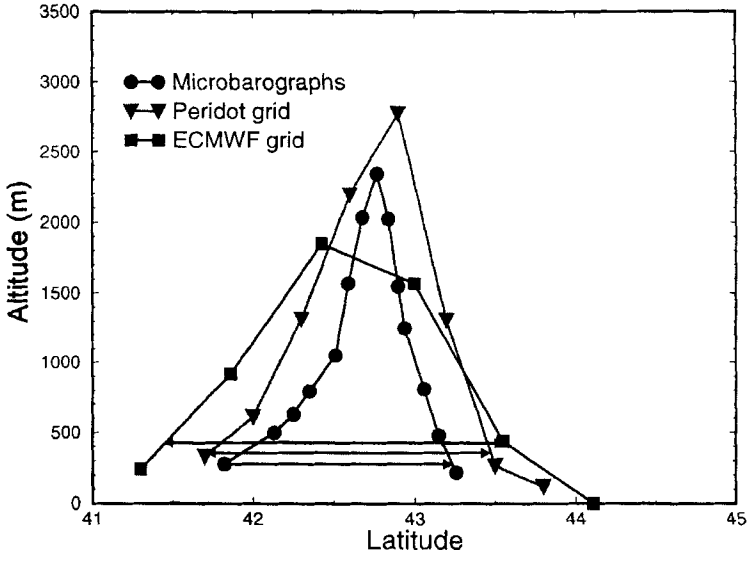


Figure 2. Orography profiles of the transects along which the pressure drags are calculated.

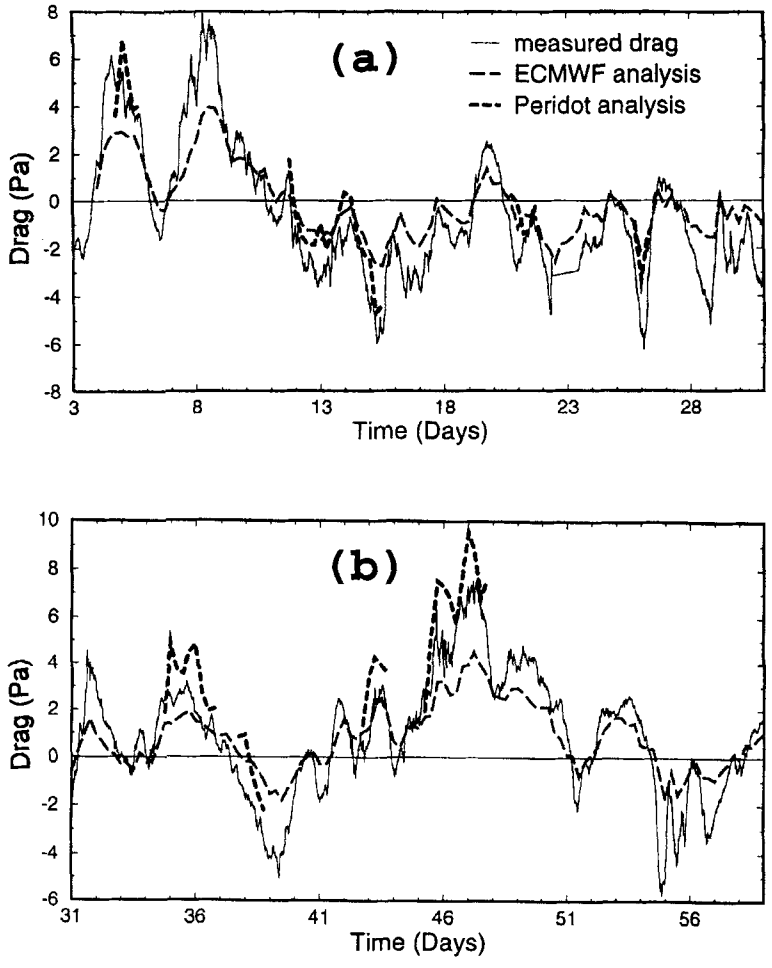


Figure 3. Measured and modelled (analysis) pressure drag during PYREX: (a) October 1990 and (b) November 1990.

can have a significant ageostrophic component. In this case, the pressure drag may follow the predictor, $D_a$.

$$D_a = \rho_0 N V \frac{(Z_{max} - Z_{min})^2}{L} \tag{6}$$

which is a typical value of the pressure drag exerted by hydrostatic gravity waves. In (6), $V$ characterizes the low-level wind component that is normal to the ridge and $N$ is the low-level buoyancy frequency. It is close to the drag an infinitesimal two-dimensional mountain of height $(Z_{max} - Z_{min})$ and of finite length $L$ exerts on a uniform non-rotating hydrostatic flow by radiating gravity waves. Nevertheless, the fact that the pressure-drag value has the order of magnitude of $D_a$, does not mean that the associated dynamics are linear steady and two dimensional. It is a typical value of the pressure drag, although the actual pressure drag can be much larger in two-dimensional nonlinear situations (Peltier and Clark 1983; Clark and Peltier 1984). It can be smaller in two-dimensional linear configurations when the Rossby number is small (Smith 1979b), when the incident flow is unsteady (Lott and Teitelbaum 1993), or when the mountain is three dimensional (Phillips 1984). In the fully nonlinear three-dimensional case, Miranda and James (1992) have shown that the drag

can be larger than its linear value when the mountain forces nonlinear breaking gravity-waves, but smaller than this value when flow splitting and separation occur behind the mountain. In any case, whatever the dominant ageostrophic behaviour, the drag has at least the magnitude of this ageostrophic predictor.

These predictors have been calculated using upstream flow structure ($U$, $V$, $N^2$) observed at the 850 hPa level in the ECMWF analysis. This rather high level was chosen in order to minimize the influence of the boundary-layer structure on the calculation of the predictors. The mean mountain height, $h_m$, as well as the maximum mountain height, $Z_{max} - Z_{min}$, are those of the ECMWF transect. The two predictors are compared with the ECMWF pressure drag in Fig. 4. It shows that during most of the campaign, the

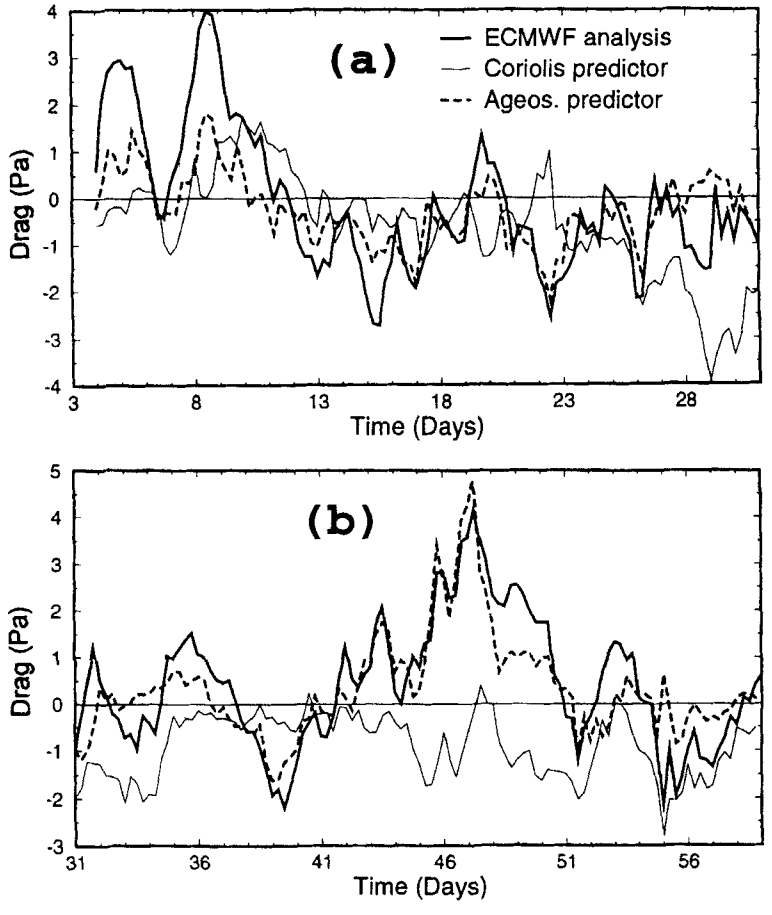


Figure 4. ECMWF (analysis) pressure drag and predictors during PYREX: (a) October 1990 and (b) November 1990.

ageostrophic predictor, $D_a$, is doing a far better job than the Coriolis predictor, $D_C$. During long periods of the experiment, the changes of the model pressure drag follow those of $D_a$ (days 4 to 9, 13 to 27, and 37 to 48). These periods include most of the peaks where the model pressure drag exceeds 2 Pa (days 8 to 9, 14 to 15, 22 to 23, 38 to 39, 43 to 44, and 46 to 50). At these peaks, the flow component perpendicular to the mountain, $V$, is large. When the wind perpendicular to the range goes to zero, the pressure drag goes to zero whatever the value of the wind parallel to the mountain, and whatever the value of

$D_C$ (the fall in the drag value from day 26 to 28 is typical of this behaviour). According to this predictor, it seems natural that the ECMWF model gives a pressure drag whose value is smaller than the measured drag, since in the ECMWF model the maximum mountain height is lower than that of the PYREX central transect (Fig. 2). It is also noteworthy that the Peridot model gives a drag amplitude which is quite accurate. In fact, the Pyrénées maximum height in the Peridot model is quite close to that of the PYREX central transect (Fig. 2). During these periods, Bessemoulin *et al.* (1993) have further shown, calculating the upstream conditions from radiosoundings and taking the mountain maximum height measured along the PYREX transect, that $D_a$ is also a good predictor of the measured drag. This means that in many cases, the missing drag in the ECMWF model can be approximated by:

$$\rho_0 N V \frac{(Z_{max} - Z_{min})^2_{\text{PYREX transect}} - (Z_{max} - z_{min})^2_{\text{model}}}{L}. \tag{7}$$

Nevertheless, there are three periods where the ageostrophic predictor is bad (days 10 to 11, 28 to 36 and 49 to 59). During these three periods, the wind normal to the mountain is often small compared with the wind parallel to the massif, and the Coriolis predictor can do a good job, compared with the model pressure drag (days 10 to 11 and 54 to 59). From days 32 to 36 and 52 to 53, $D_C$ is poor compared with the measured drag, but its variations in time follow that of the actual drag quite well. Going back to the measured drag (Fig. 3), it appears that two peaks, where the measured drag exceeds 4 Pa (days 32 and 55), occur during these along-ridge cases. At these peaks, the model drag is nearly three times smaller than the measured drag. The model is clearly much more in error during the along-ridge cases than it is during the normal-ridge cases. This along-ridge drag deficit is particularly spectacular at the end of November (days 54 to 59).

Among this very large range of cases, it appears that three typical situations deserve special attention. In the first one, the wind perpendicular to the ridge is strong and the model pressure drag is large and well predicted by $D_a$. It shows that the ECMWF model has a significant ageostrophic response, and that the drag amplitude is mainly related to the mountain maximum elevation. This explains why the ECMWF model pressure drag is too small. In the second situation, the wind is nearly parallel to the mountain, and the pressure drag is small, contrary to what should be expected from $D_C$. This occurs during the periods of the experiment where the variations of the model drag follow the variation of $D_a$. In the third situation, the wind is also parallel to the mountain, the pressure drag is not zero and $D_C$ explains the amplitude of the model pressure drag. In this case, the model pressure drag is related to the mean mountain elevation, and it is small when compared with the measured pressure drag, even though the mountain mean elevation is at least as large (in fact even larger in the ECMWF model since an envelope orography is used) as that of the actual orography. This means that an important part of the missing drag is related to lift mechanisms which are not represented in the model, and which cannot be explained by the mechanism described by Smith (1979a). It seems quite clear that a better theoretical understanding of these large lift states would help to determine whether these effects can be (or need to be) parametrized in general-circulation models.

### (c) *Other drag processes related to subgrid-scale effects*

To determine whether the pressure-drag deficits of the ECMWF model are compensated for by the parametrization schemes, Fig. 5 shows the gravity-wave drag, and the boundary-layer drag, obtained from forecasts, averaged over 12 h periods and over the model transect. Throughout the PYREX period, the subgrid-scale gravity-wave drag is small when compared with the resolved pressure drag. For the Pyrénées, it does not com-

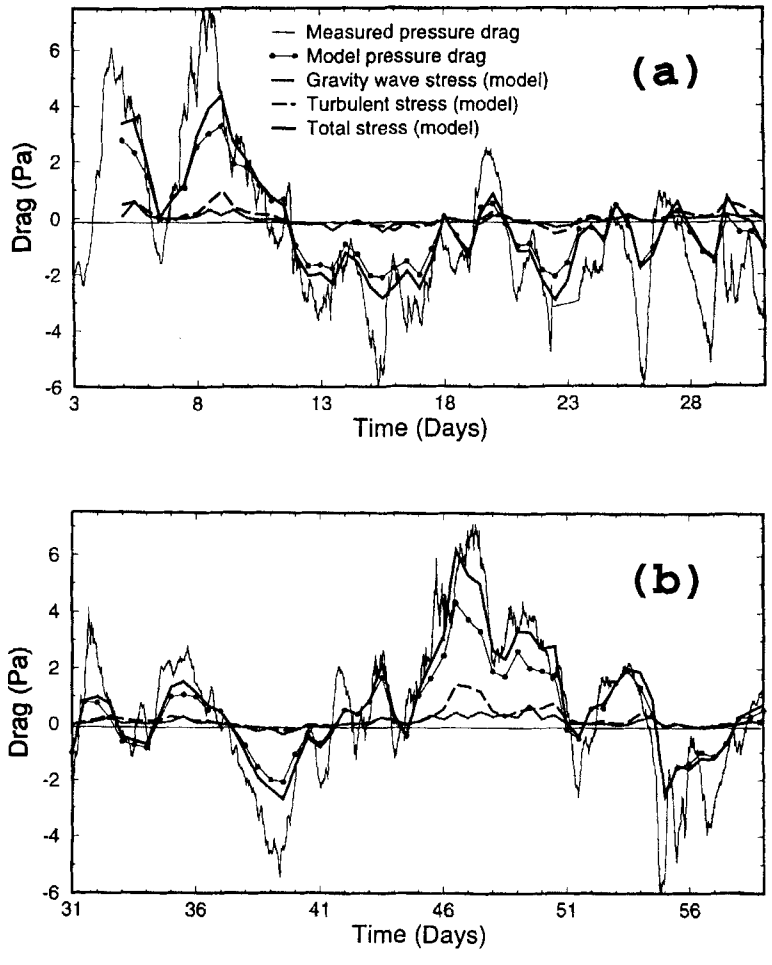


Figure 5. Pyrénées mountain drag observed in ECMWF short-term forecasts during PYREX compared with the measured pressure drag. In the forecasts, the total mountain drag is the sum of the explicit pressure drag, the parameterized boundary-layer drag and the parameterized gravity-wave drag. (a) October 1990 and (b) November 1990.

pensate for the difference between the model pressure drag and the observed drag. The amplitude of the boundary-layer drag is often larger than the gravity-wave drag. Nevertheless, even if both drags are added to the pressure drag, it is clear that the model still underestimates the measured drag. In some cases, this total model drag does a significantly better job than the model pressure drag alone. This is mainly true when the wind is perpendicular to the massif and very strong (days 46–47). Then the boundary-layer scheme imposes a strong surface friction related to the rather high roughness length ($z_0 = 10$ m), typically existing over the Pyrénées. For such a roughness length, Grant and Mason (1990) found significantly larger drag than that found here. This is not, however, in contradiction with the model boundary-layer-drag value, since in most of the cases presented here, the boundary layer is stable and the turbulent diffusion is significantly smaller than in the neutral configuration studied by Grant and Mason. When the wind is parallel to the massif, all the friction perpendicular to the massif goes to zero and the lift drag is always underestimated by the model.

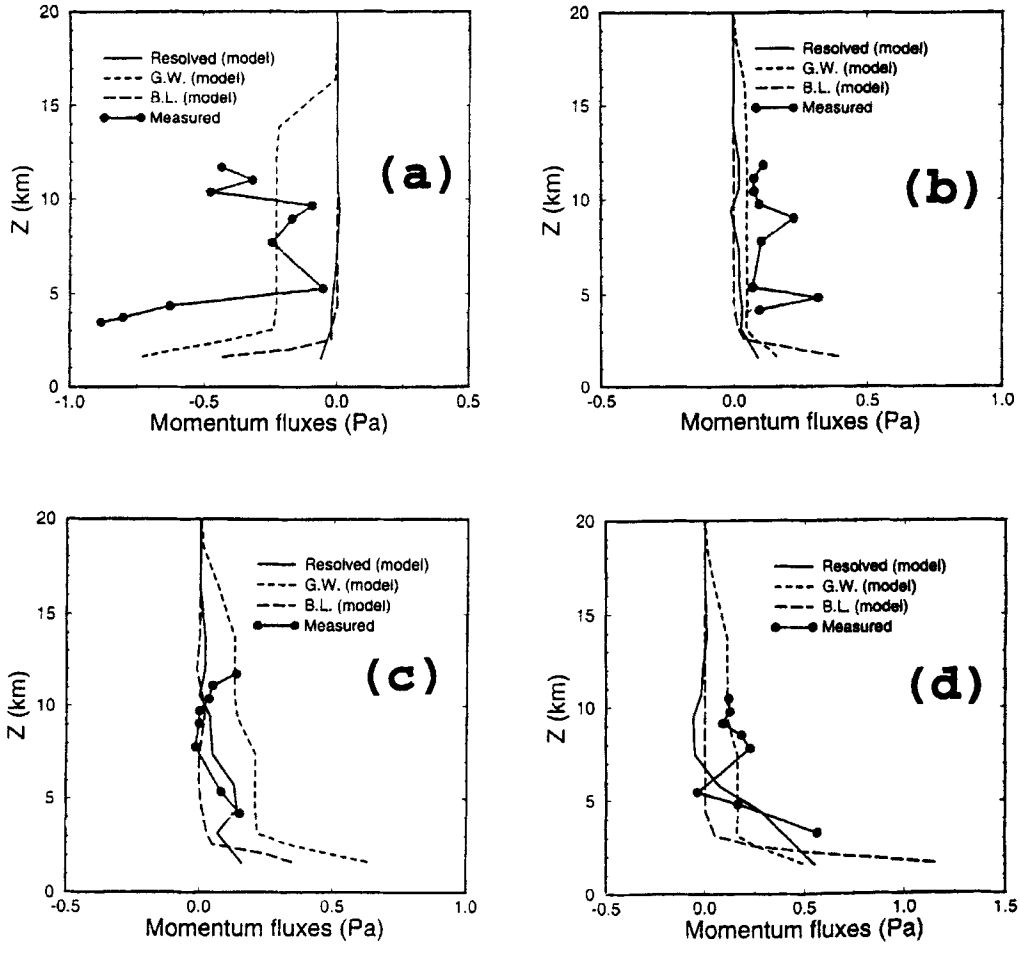


Figure 6. Measured and ECMWF (forecast) model meridional momentum flux vertical profile during PYREX: (a) 06 UTC 15 October 1990, (b) 12 UTC 14 November 1990, (c) 06 UTC 15 November 1990 and (d) 06 UTC 16 November 1990. (G.W. is gravity wave and B.L. is boundary layer.)

Figure 6 shows the vertical flux of momentum calculated from aircraft measurements taken above the central transect (Bougeault, private communication) together with the resolved and parametrized model meridional momentum fluxes. The model fluxes were calculated over the same transect as the model pressure drag. The measured fluxes (Bougeault, private communication) were calculated from detrended observed perturbations of the velocity components. In the model, the explicit momentum flux has also been calculated from detrended perturbations of the model velocity components interpolated at pressure levels. The subgrid-scale orographic fluxes were calculated after interpolation of the model level subgrid-scale fluxes to pressure levels. In some cases, the measured fluxes have a strange behaviour. For example, negative values exist just above 5 km on 16 November 1990. This is difficult to explain and implies that aircraft data should be handled with care, at least at low levels. This is also true when trapped lee waves are present, as these can propagate downstream, far away from the location of the transect, making the interpretation of the fluxes measured above the central transect difficult. For the four dates presented, it is found that the vertical flux of momentum is very small when compared

with the pressure drag. This is true for the data as well as for the model fluxes. This is noticeable, since in most of the cases presented here, there is no wave breaking (except in the ECMWF model for 06 UTC 15 October 1990), meaning that the flow is predominantly decelerated at low levels (i.e. below or close to the mountain top). Accordingly, the measured fluxes show a strong increase when approaching the ground. In the model, this low-level drag is partly represented in the gravity-wave drag scheme. Nevertheless, it is important to note that this low-level drag decelerates the flow in the model significantly below the actual mountain top, while in the measurements similar drags are observed above the actual mountain top. This means that the low part of the subgrid-scale gravity-wave scheme should also decelerate the flow at higher levels than it presently does. On the other hand, it is noticeable that the gravity-wave drag scheme is often doing quite a good job in the upper levels. It seems that there is no need to change its amplitude there. Figure 6 also shows the parametrized turbulent-stress profile, which gives significant drag in the low levels of the model.

## 4. Two along-ridge cases

In this section, the synoptic flow in two typical along-ridge cases is described and related to the model pressure drag. For the first, the model drag is zero, as is the measured drag, while $D_C$ is not zero (18 UTC 26 October 1990). For the second, the model drag is negative and small compared with the measured drag, but it is well predicted by the Coriolis predictor (12 UTC 24 November 1990). Figure 7 shows the 500 hPa geopotential and 850 hPa temperature field in the vicinity of the Pyrénées for the two dates. The geopotential patterns at 500 hPa are similar with a low centred over the south-west of England maintaining a strong eastward flow over the Pyrénées. At 850 hPa, the upstream winds are also similar, and the values of $D_C$ are close (Fig. 4, times = 26.75 days and 55.5 days). As shown in Fig. 7, the main difference between these two events lies in the 850 hPa temperature field. In the situation with no drag (18 UTC 26 October 1990), a cold front is present above the massif. It is also important to note that this cold front was advancing with the low, and has not been modified very much by the local orography. In this case, the Coriolis drag can be partly balanced by a hydrostatic pressure-drag mechanism (Bessemoulin *et al.* 1993) which results from the lower air-mass density differences related to the temperature differences between the two sides of the massif. To give an idea of the temperature difference, $\Delta T_{850}$, necessary to reduce to zero the drag in the along-ridge configurations, it is useful to consider an along-ridge wind, $U = 13\ \mathrm{m\ s^{-1}}$, characteristic of the two cases presented here. This wind results, in a barotropic context, in a pressure drag given by the Coriolis predictor, $D_C \approx -2$ Pa. In the presence of a cold front with a temperature difference between the two ends of the transect of $\Delta T_{850}$, this barotropic drag can be corrected by integrating the hydrostatic equation from 850 hPa to the ground at both ends of the transect to give the resulting drag:

$$D \approx D_C - \frac{\Delta T_{850}}{2T_{850}} \frac{P_{850}}{R_d T_{850}} g Z_{850} \frac{h_m}{L}. \tag{8}$$

In (8), $T_{850}$ and $gZ_{850}$ represent the temperature and geopotential at 850 hPa, respectively, and $R_d$ is the gas constant for dry air. This hydrostatic correction can balance the $-2$ Pa Coriolis pressure drag for $\Delta T_{850} \approx -6$ K. As shown in Fig. 7, it is close to the temperature difference observed at 18 UTC 26 October, when the model pressure drag is close to zero. On the other hand, on 24 November, the across-ridge temperature difference does not exceed 1 K, and the model drag is close to $D_C$.

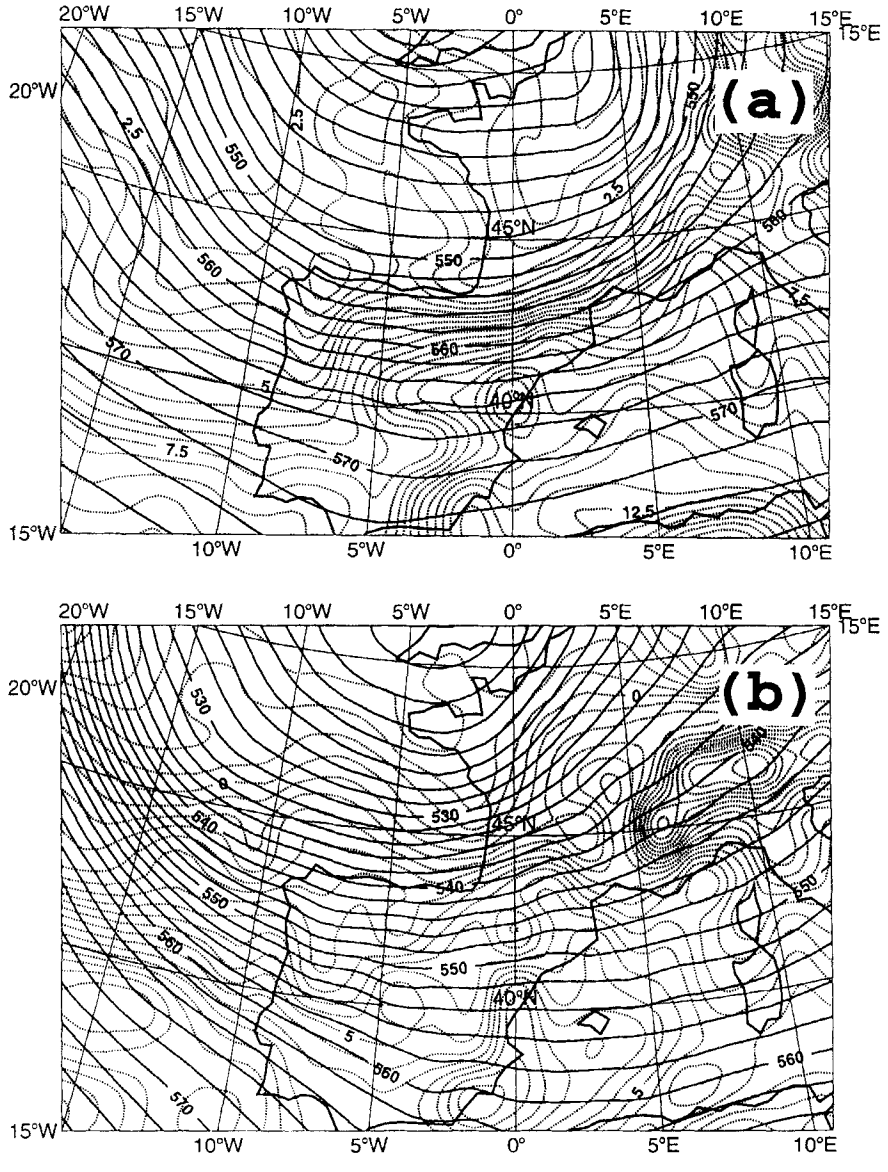


Figure 7. ECMWF analysis. 500 hPa height (solid line; contour interval = 10 m) and 850 hPa temperature (dotted line; contour interval = 1 K) for the two along-ridge cases: (a) 18 UTC 26 October 1990 and (b) 12 UTC 12 November 1990.

From a dynamical point of view, it is well known that the nature of the flow field near a mountain strongly depends on the way the isentropic surface intersects it (Smith 1979a). For instance, most theoretical studies of mountain flow, and particularly the quasi-geostrophic theories, assume that the incident flow is barotropic, and the resulting ground potential temperature is constant. As shown in Fig. 8, this is not the case at all in both situations discussed here. At both times, 18 UTC 26 October 1990 and 12 UTC 24 November 1990, the isentropes intersect the ground. In fact, when there is no drag, the front is much more inclined than the mountain slope (it is more vertical). In a given potential temperature ($\theta$) layer, the flow does not go around the obstacle. On the other hand, when the drag is

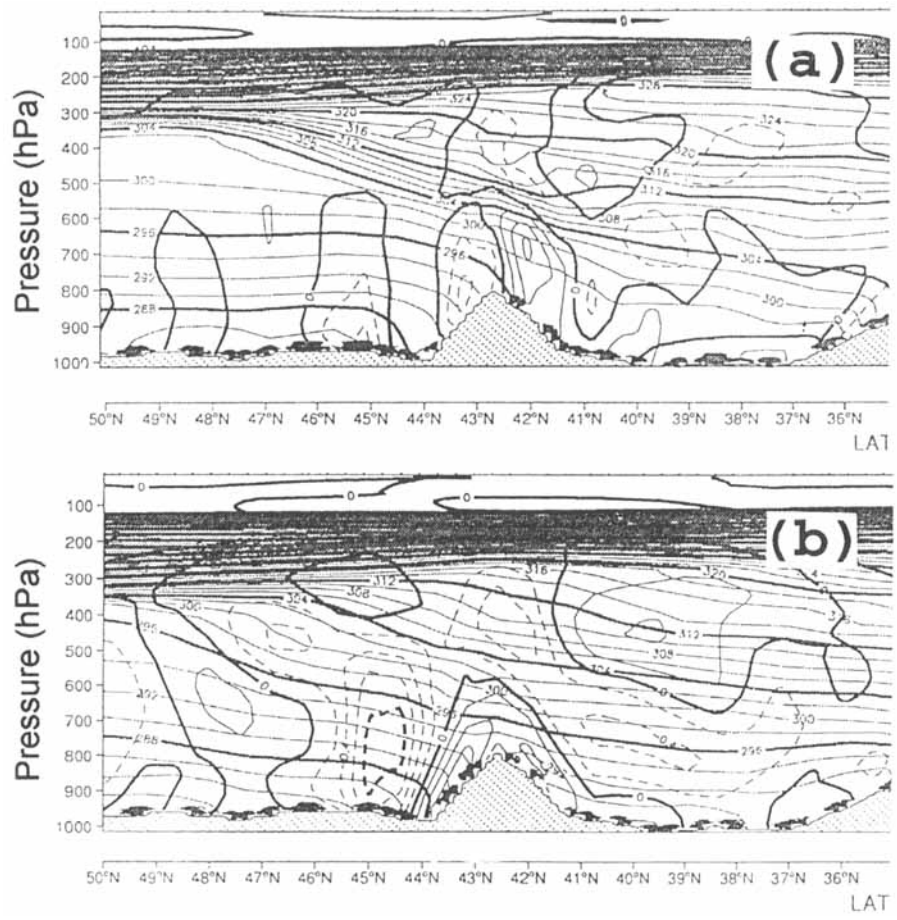


Figure 8. Meridional vertical section (1°E) of the pressure tendency (contour interval = 0.2 Pa $s^{-1}$, negative values dashed) and potential temperature (contour interval = 1 K) issued from ECMWF forecasts of the two along-ridge cases: (a) 18 UTC 26 October 1990 and (b) 12 UTC 24 November 1990.

not zero, the isentropes are less inclined than the mountain slope and the flow, within a given isentropic layer, goes around the obstacle.

## 5. Two normal-ridge cases

As discussed in section 2, for the normal-ridge events there is some evidence that the pressure-drag value is related to 'low' level flow dynamics (here again, 'low' means near and below the actual mountain top). According to theoretical studies, three kinds of low-level processes can be related to the drag. The first is the occurrence of strong downslope winds in the lee of the massif (Smith 1985), the second is the onset of blocking on the windward side of the mountain (Pierrehumbert and Wyman 1985) and the third is that of wake production (Schär and Smith 1993). In any case, these processes have to be seen as independent from one another. For instance, theoretical studies show that when the flow goes over the mountain, a strong föhn can drive a hydraulic jump, which in the three-dimensional case will result in a wake (Miranda and James 1992). When the flow goes around the mountain, flow separation generally occurs on the mountain flanks, which also leads to a wake. In both cases a certain amount of incident flow retardation

and blocking occurs upstream. To determine if these phenomena occur in the numerical models considered herein, the flow can be described on low-level isentropic surfaces. In such diagnostics, the flow goes around the mountain if the isentropes intersect the ground; it goes over the mountain if the isentrope does not intersect the ground. The occurrence of strong downslope winds will result in a descent of the $\theta$-surfaces, below their upstream altitude. The onset of blocking will result in a piling up of the fluid on the windward side which will elevate the isentropes. The occurrence of wakes will be characterized by isentropic vorticity production, and a significant difference in the value of the Bernoulli function between the two sides of the ridge (Schär and Smith 1993).

All these processes are known to occur when the non-dimensional mountain height, $H_{ND} = Nh/V$, is larger than one. In the ECMWF model, for the Pyrénées, it has a typical value of $H_{ND} = 1.7$ when the wind perpendicular to the mountain, $V$, is 10 m s$^{-1}$, and when the buoyancy frequency, $N$, is 0.01 s$^{-1}$. Although it fluctuates significantly around this value, it always remains close to one, since the mountain elevation in the ECMWF model, $Z_{MAX} - Z_{MIN} = 1600$ m, is quite high. In the Peridot model, as well as for the actual flow, the non-dimensional mountain height is larger, $H_{ND} = 2.5$, within the same typical configuration. In the rotating case, the flow dynamics are also controlled by the Rossby number, $Ro = V/fL'$, where, following Pierrehumbert and Wyman (1985), $L'$ is the mountain half width, $L' = L/2$. It is close to unity in the models as well as in reality. Therefore, although the Coriolis force should play a role, ageostrophic dynamics will be dominant. It is also true that the condition $RoH_{ND} \geqslant 1$ is satisfied, which means that upstream blocking can occur but will be limited to a distance, $L_d \approx \text{Min}(N(Z_{MAX} - Z_{MIN})/f,\ L_x) \approx 150$ km, upstream of the Pyrénées (Pierrehumbert and Wyman 1985), $L_x$ being the along-ridge length of the mountain.

In the following, two situations of this type are presented. In the first one (12 UTC 15 October 1990) the incident flow is from the south-west and the total mountain drag is smaller than the measured pressure drag. In this situation some aspects of the flow dynamics in the ECMWF model are quite incorrect. It highlights important problems with the model. In the second situation (06 UTC 15 November 1990) the total mountain drag in the ECMWF model is quite close to the measured drag. In this case, the contribution of the boundary-layer drag to the total mountain drag is quite large (Fig. 5, day 46.25) and the combination of the resolved dynamics and the parametrized processes leads to realistic low-level dynamics.

### (*a*) *PYREX PO13: 12* UTC *15 October 1990*

*Peridot model.* Figure 9 shows fields from the Peridot analysis on the $\theta = 302$ K surface. The shaded zones correspond to the areas where the lowest model-level potential temperature is smaller than 302 K. It indicates the intersection between the $\theta$-surface and the ground. As shown in Fig. 9(a), the wind field indicates that on the windward side the flow passes round the Pyrénées. There, it is deflected toward both flanks of the massif. On the leeward size, a relatively calm zone is present. This calm zone is surrounded by two vorticity bands of opposite sign (Fig. 9(c)), which extend over approximately 300 km, in the lee of the massif. It has been verified that these vorticity anomalies correspond to potential-vorticity anomalies, indicating flow detachment on the mountain flank with a wake formation downstream. The occurrence of the wake is confirmed by looking at the Bernoulli function (Schär and Smith 1993):

$$B = C_p T + gZ + \frac{u^2 + v^2}{2} \tag{9}$$

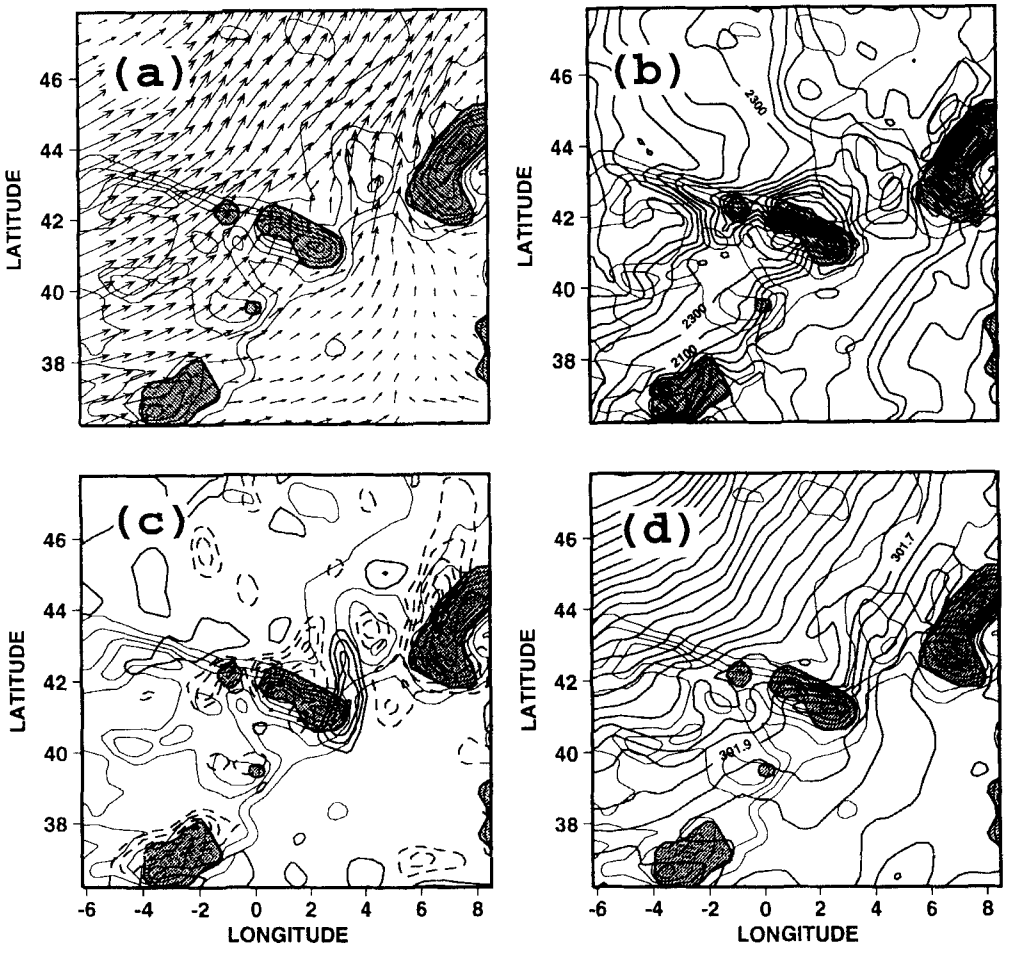


Figure 9. Peridot analysis, 12 UTC 15 October 1990. Orography (contour interval = 400 m) and flow diagnostics on the isentropic surface $\theta = 302$ K. In the shaded area, the isentrope goes below the lowest model level. (a) wind; (b) elevation, contour interval = 200 m; (c) isentropic relative vorticity, contour interval = $0.5 \times 10^{-4} s^{-1}$, negative values dashed and (d) Bernoulli function, contour interval = 100 J $kg^{-1}$.

which like potential vorticity is a conserved quantity for adiabatic flow in the absence of body forces. In (9), $C_pT$ approximates the enthalpy per unit mass and $gZ$ is the geopotential height. The wake itself is characterized by a pool of fluid with a Bernoulli-function deficit, which is located away from the vorticity-producing area (Fig. 9(d)). Away from the Pyrénées and the Alps, the Bernoulli-function isolines nearly follow the wind streamlines, indicating a small amount of dissipation or diabatic heating. The map of the $\theta$-surface elevation (Fig. 9(b)) also shows some blocking upstream, where it presents a significant maximum. It is noteworthy that this local maximum of the isentrope elevation does not extend further upstream than 150 km. This indicates that the three dimensionality of the obstacle limits the extent of the blocking, because the flow can go around the mountain rather than piling up on its upstream side. This behaviour, together with the extension of the blocked zone, agrees with the scale analysis of the blocking-zone extension done by Pierrehumbert and Wyman (1985). On the lee side, a significant minimum in the $\theta$-surface height indicates the onset of föhn.

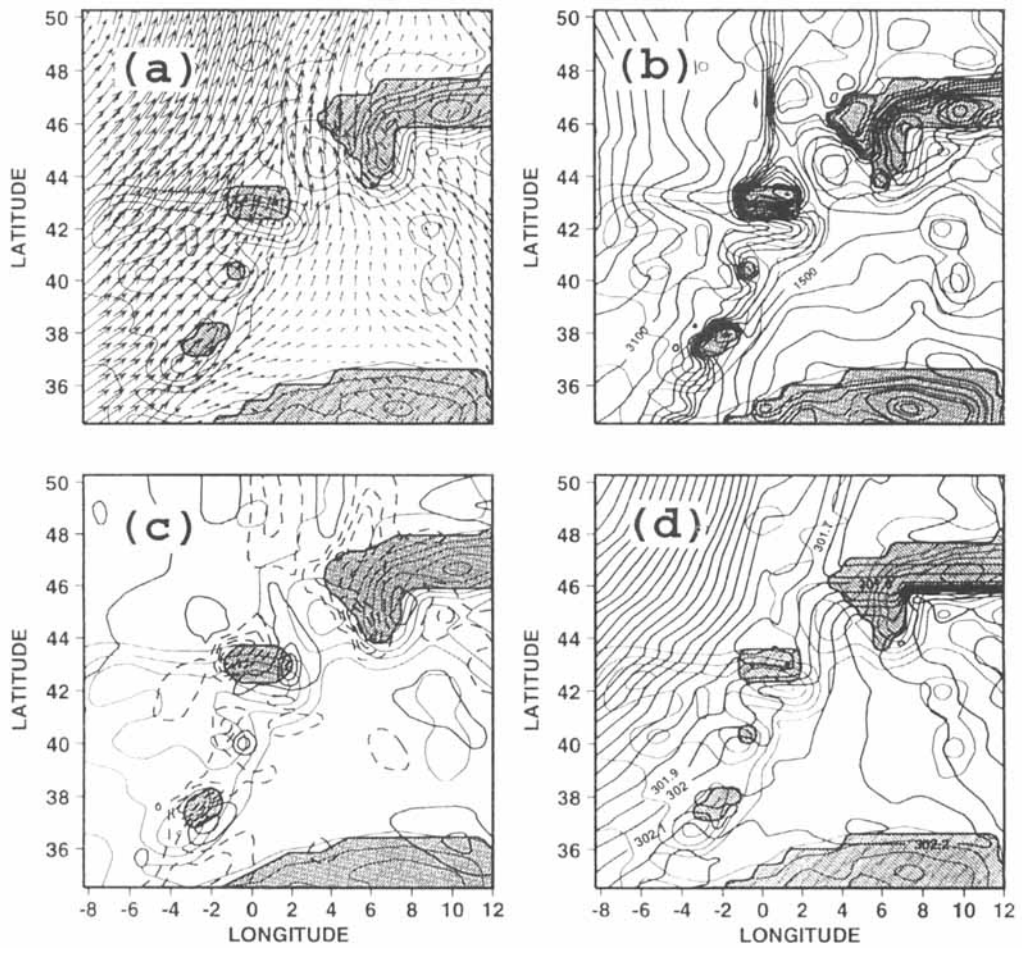


Figure 10. ECMWF 12 h forecast, 12 UTC 15 October 1990. Orography (contour interval = 400 m) and flow diagnostics on the isentropic surface $\theta = 302$ K. In the shaded area the isentrope goes below the lowest model level. (a) wind; (b) elevation, contour interval = 200 m; (c) isentropic relative vorticity, contour interval $= 0.5 \times 10^{-4} s^{-1}$, negative values dashed; and (d) Bernoulli function, contour interval = 100 J kg$^{-1}$.

*The ECMWF model.* In the ECMWF model, the isentropic surface $\theta = 302$ K (Fig. 10) also seems to intersect the Pyrénées. At levels above 303 K the fluid does not intersect the mountain in the ECMWF model, whereas intersection occurs up to $\theta = 306$ K in the Peridot model. This is mainly due to the difference in elevation of the Pyrénées between the two models. Furthermore, at this level, it appears that the flow does not pass round the mountain in the ECMWF model. The wind field (Fig. 10(a)) on the windward side of the mountain is not deflected around the intersection area between the isentrope and the mountain. It appears that the föhn forces the isentrope to go very close to the ground, below the first model level, but no real intersection between the isentrope and the mountain occurs. As in the Peridot analysis, the Bernoulli function shows a deficit between the two sides of the Pyrénées (Fig. 10(d)). In the ECMWF model, since this cannot be related to flow detachment on the mountain flanks, it has to be due to the diabatic mixing and the frictional body forces which can be large at low levels. Nevertheless, the model behaviour seems quite inconsistent. In fact a Bernoulli deficit along the flow means that the diabatic processes and the non-conservative forces have driven a potential-vorticity flux perpendicular to the flow

(in the steady case, the Bernoulli function is the stream function of the absolute-vorticity flux (Schär (1993))). As shown on Fig. 10(c), the vorticity anomalies are quite small away from the immediate vicinity of the mountain flanks.

At levels which do not intersect the massif, the impact of the subgrid-scale parametrized forcing on the resolved dynamics can be further analysed, applying the generalized potential-vorticity conservation theorems (Haynes and McIntyre 1987). In the hydrostatic approximation, used in all the models discussed herein, the isentropic absolute-vorticity flux is given by:

$$\mathbf{u}(\zeta_{r\theta} + f) + \mathbf{k} \times \mathbf{F} - \mathbf{k} \times \dot{\theta} \frac{\partial \mathbf{u}}{\partial \theta} \tag{10}$$

where the term

$$\mathbf{k} \times \mathbf{F} - \mathbf{k}\dot{\theta} \frac{\partial \mathbf{u}}{\partial \theta} \tag{11}$$

represent the isentropic absolute-vorticity flux due to the non-conservative force, and the diabatic heating respectively. In (10) and (11), $\mathbf{u}$ and $\zeta_{r\theta}$ are the isentropic wind and the isentropic relative vorticity respectively, $\mathbf{k}$ is the vertical unit vector, $f$ is the planetary vorticity, $\mathbf{F}$ and $\dot{\theta}$ represent the body force and the diabatic processes related to the parametrization schemes, respectively. Both fluxes (10) and (11) are shown on the surfaces $\theta = 302$ K and $\theta = 304$ K in Fig. 11. At both levels it appears that non-advective contributions to the vorticity flux exist above and to the lee of the mountainous areas. On the lee flank of the mountains, the föhn forces the isentropes to go close to the ground (Fig. 11(c)) where it experiences low-level gravity-wave drag, enhanced boundary-layer drag and diabatic forcing. Nevertheless, on the Pyrénées, the non-advective potential-vorticity flux is significantly smaller than the total potential-vorticity flux. This non-advective forcing results in a Bernoulli deficit shown in Fig. 11(d). Nevertheless, this deficit has too sharp a gradient above the Pyrénées because the absolute-vorticity fluxes are far from being a tangent to the isolines of the Bernoulli function. This kind of discrepancy is often observed in the model. It also occurs at higher levels (i.e. in the mid-troposphere), where no significant subgrid-scale forcing acts while small Bernoulli-function deficits across the Pyrénées occur. This means that the dissipative processes and the diabatic processes are not completely determined by the subgrid-scale parametrization schemes. Furthermore, some sensitivity experiments were done, decreasing the horizontal diffusion in the model by a factor of 10, resulting in flow patterns which are very close to those described previously. None of the explicit model dissipations can explain the deficit of the Bernoulli function. In this case, where the model has a significant ageostrophic response whose scale is close to the model truncation, a significant part of the energy dissipation is numerical.

In the ECMWF model, the flow splitting and the downstream wake are underestimated mainly because the mountain is too low. According to theoretical studies this leads to overestimation of gravity waves and to underestimation of flow splitting. The structure of the gravity waves for this case is shown in Fig. 12(b) which presents features, such as the phase tilt in the vertical, which are characteristic of mountain gravity waves. It also shows again the significant nonlinear behaviour already described, like the intense föhn on the downstream side of the massif. The aforementioned model discrepancies between the explicit energy dissipation in the model and the Bernoulli-function deficit can be interpreted as a spurious numerical damping of this wave pattern. Sometimes this overestimation of the wave signal in the model can lead to features which are not observed. For example, at 06 UTC 15 October (Fig. 12(a)), the model mountain wave is breaking in the lee of the mountain between 750 hPa and 650 hPa. In this case, the wave amplitude

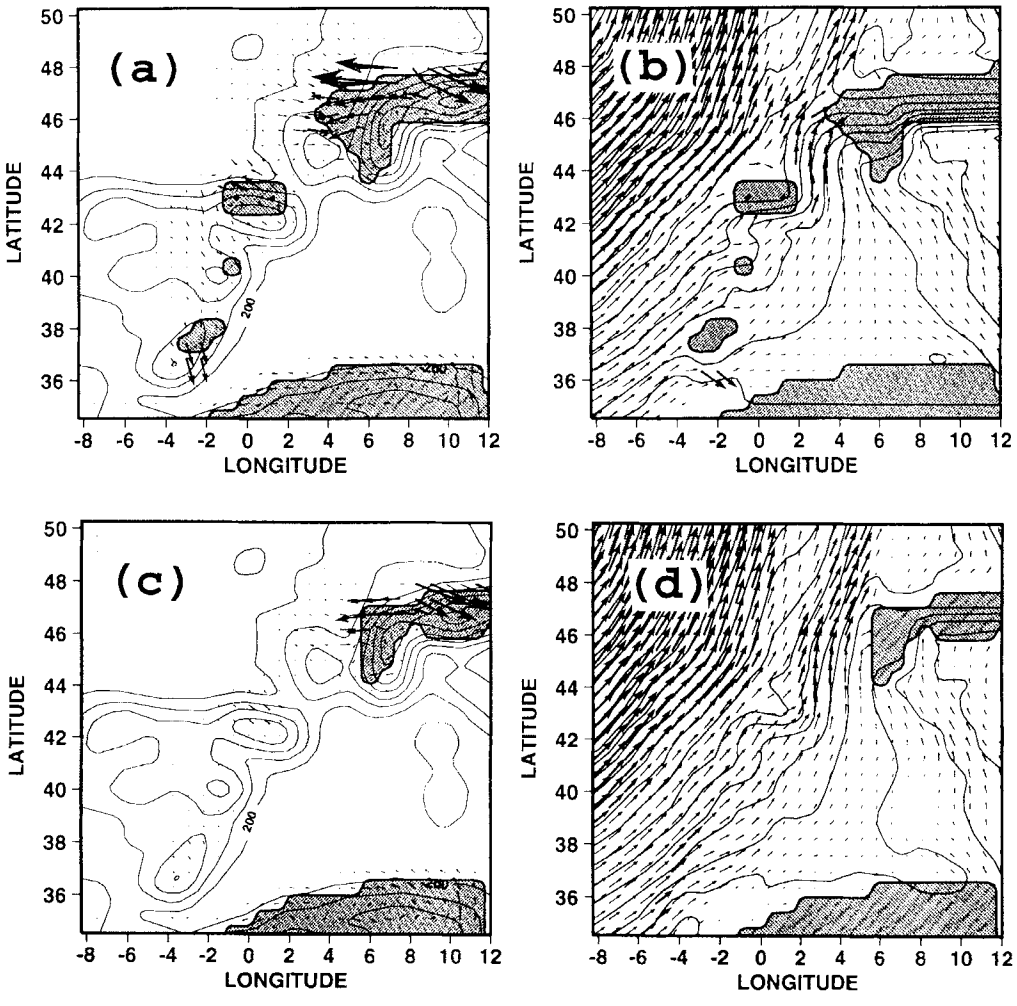


Figure 11. ECMWF 12 h forecast, 12 UTC 15 October 1990. Isentropic potential-vorticity fluxes. In the shaded area the isentrope goes below the lowest model level. Orography and potential-vorticity fluxes due to the parametrized frictional forces and diabatic heating: (a) 302 K and (c) 304 K. Bernoulli function (contour interval = 100 J $kg^{-1}$) and total potential-vorticity flux: (b) 302 K and (d) 304 K.

is largest below the breaking level. This means that wave absorption and presumably nonlinear wave reflection is occurring there, in agreement with the very small value of the resolved momentum flux shown in Fig. 6(a) for this date. It is noteworthy that this long-wave breaking was not observed during the field experiment (Bougeault *et al.* 1993).

The observation of such a significant ageostrophic wave pattern above mountains in the ECMWF model has became frequent since the introduction of the truncature T213 in the forecasting system. Nevertheless, according to the discrepancies in the dissipation terms described earlier and to the fact that the momentum fluxes carried by those waves are always very small when compared with the pressure drag (in many cases the waves in the model show a nearly linear behaviour for which the pressure drag and the wave momentum flux should be closer then they presently are), it appears that this ageostrophic pattern is not always properly controlled by the model.

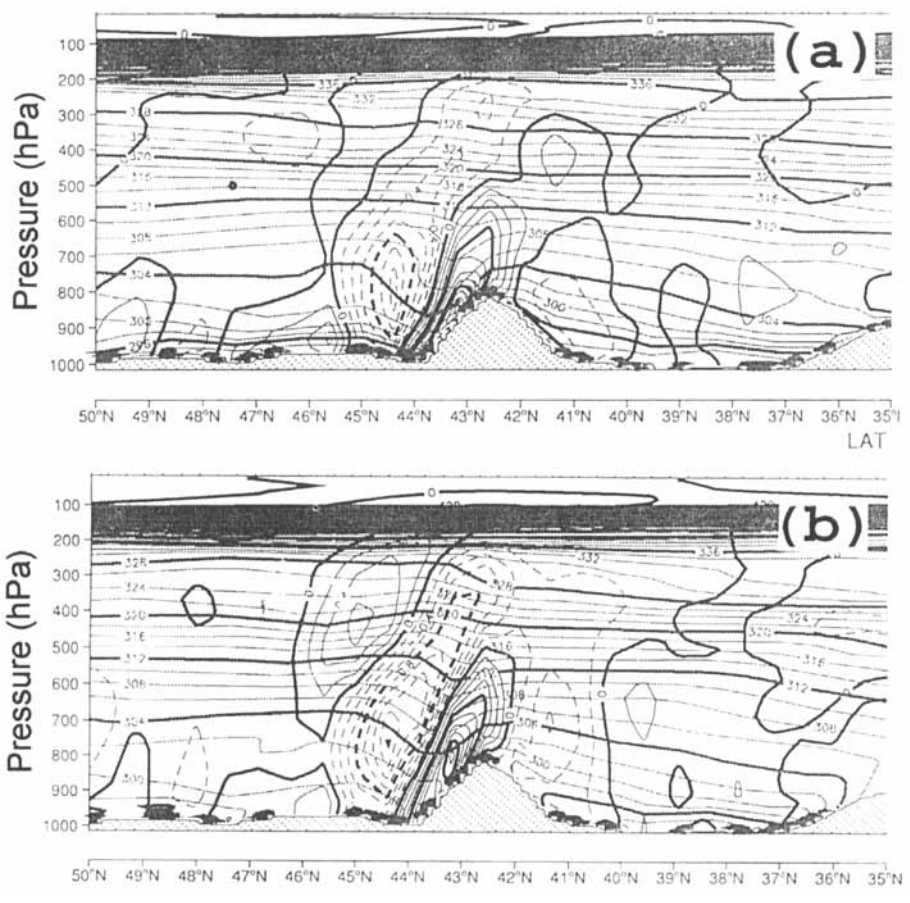


Figure 12. Meridional-vertical section (1°E) of the pressure tendency (contour interval = 0.2 Pa $s^{-1}$, negative values dashed) and of the potential temperature (contour interval = 1 K) issued from ECMWF forecasts: (a) 06 UTC 15 October 1990 and (b) 12 UTC 15 October 1990.

### (*b*) *PYREX POI9: 06* UTC *15 November 1990*

*Peridot model.* Figure 13 shows the different isentropic flow fields analysed with the Peridot model on the $\theta = 293$ K surface. It corresponds to a surface which still intersects the Pyrénées in the Peridot model, but which does not in the ECMWF model. The main features described for POI3 are found again. Significant flow splitting upstream of the massif can be observed in the velocity fields. Flow detachment occurs on the eastern flank of the mountain together with a wake characterized by a long negative vorticity band extending from the eastern flank of the mountain, over the so called Gulf of Lyons, Mediterranean zone. The onset of flow separation is further confirmed by the significant fall in the value of the Bernoulli function between the two sides of the mountain. The $\theta$-surface elevation map also shows significant föhn downstream.

*ECMWF model.* At the $\theta = 293$ K level (Fig. 14), the ECMWF model follows many of the processes occurring in the Peridot model. Although no flow splitting occurs, since the isentrope does not intersect the mountain, the vorticity band downstream, as well as the Bernoulli-function difference between the two sides of the chain are well represented. Nevertheless, contrary to what occurs in the Peridot analysis, the wake in the ECMWF

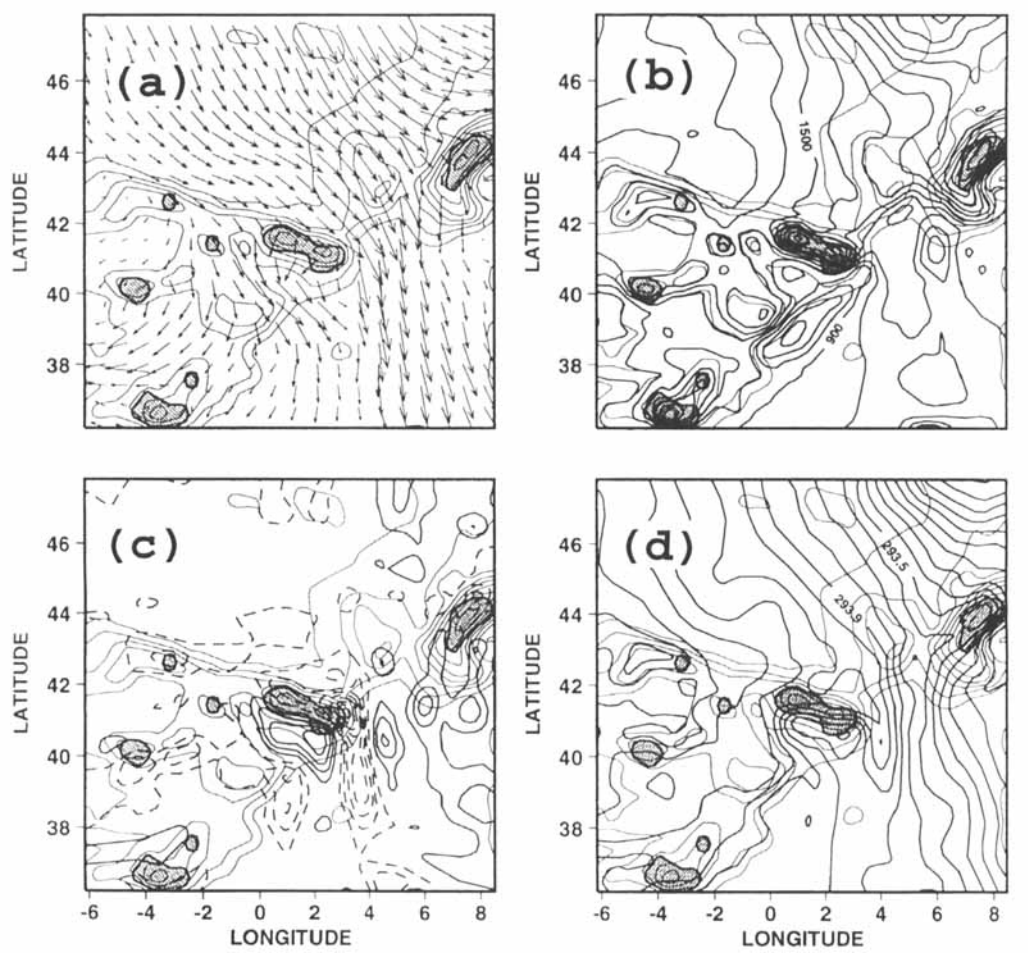


Figure 13. Peridot analysis, 06 UTC 15 November 1990. Orography (contour interval = 400 m) and flow diagnostics on the isentropic surface $\theta = 293$ K. In the shaded area the isentrope goes below the lowest model level. (a) Wind, (b) elevation (contour interval = 200 m), (c) isentropic relative vorticity (contour interval = $0.5 \times 10^{-4} s^{-1}$, with negative values dashed), and (d) Bernoulli function (contour interval = 100 J $kg^{-1}$).

model can only be related to an interaction between the resolved flow dynamics and the parametrization schemes. Figure 15 shows the non-advective absolute-vorticity fluxes related to the parametrized non-conservative forces and diabatic heating, as well as the total fluxes of absolute vorticity and the Bernoulli head. As seen in Fig. 15(a), the non-advective contribution to the isentropic vorticity flux is large, and goes from the east of the Pyrénées towards the west. It explains the vorticity dipole shown in Fig. 14(c). Figure 15(b) further shows that the total absolute-vorticity flux follows the contours of the Bernoulli function very closely. This is particularly striking above the Pyrénées where the flow, although partly deflected, remains mainly oriented from the north-west toward the south-east and crosses perpendicularly the Bernoulli lines. In this case, in the ECMWF model, the low-level parametrized processes, together with the explicit model ageostrophic pattern, lead to a realistic wake on an isentropic surface which does not intersect the mountain in the model, while it does in the mesoscale model.

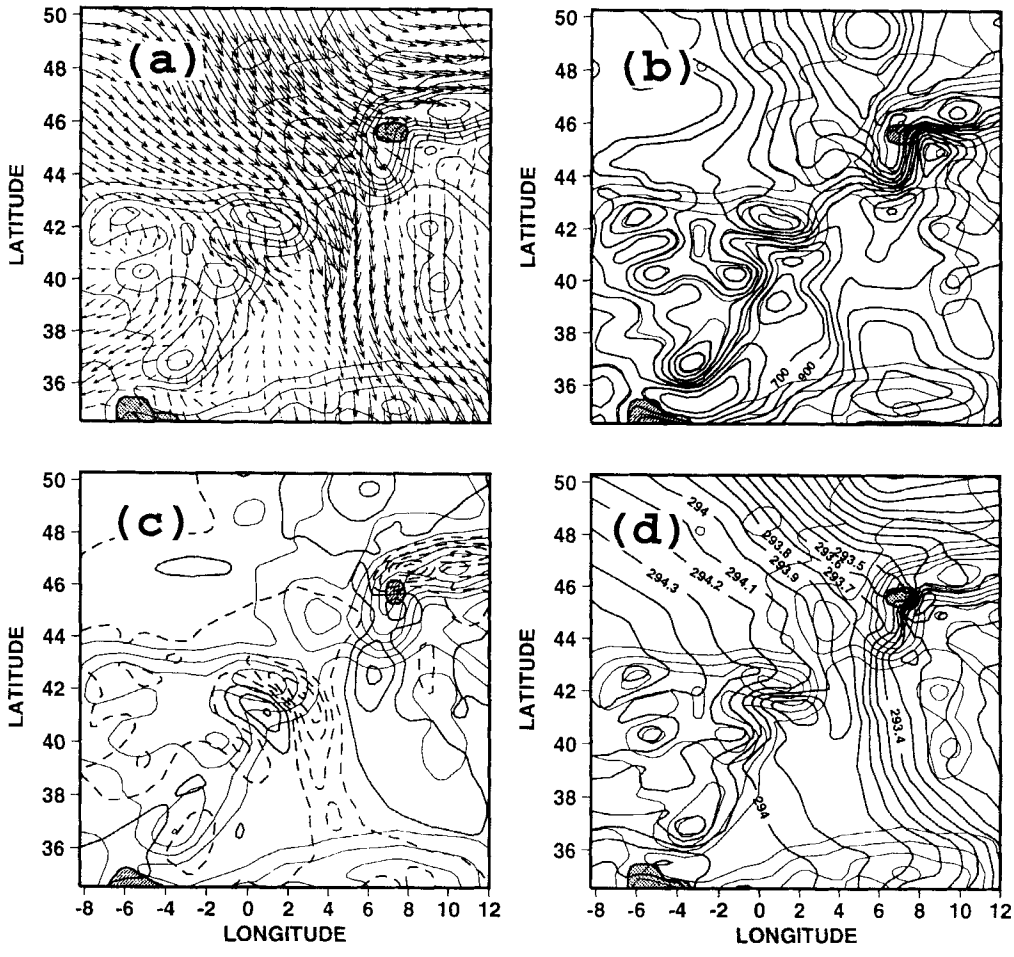


Figure 14. As Fig. 13 but for ECMWF 6 h forecast for 06 UTC 15 November 1990.

## 6. Conclusions

This paper has addressed issues that concern the representation of mesoscale orography in a global weather-prediction model by comparing the ECMWF model performance near the Pyrénées to the PYREX database. It has been shown that the model-mountain pressure drag correlates well with the measured pressure drag, but is always too small. The behaviour of the model pressure drag was interpreted using two simple drag predictors. The first is a Coriolis drag predictor related to the wind parallel to the mountain, and to the mountain mean elevation. The second is an ageostrophic drag predictor, related to the wind perpendicular to the mountain, and to the mountain maximum height. When the wind perpendicular to the mountain is small, the model pressure drag behaves like the Coriolis predictor, provided that the temperature gradient across the massif is small. For these, the pressure drag is underestimated by the model, and the subgrid-scale parametrization scheme, which has no direct lift effects, does not make up the difference between the model pressure drag and the measured drag. Also, the missing lift mechanism exerted by the mountain on the flow remains unclear. In fact, the only theory about mountain-lift drag in the atmosphere (Smith 1979a) relates it to the mountain volume, which is larger

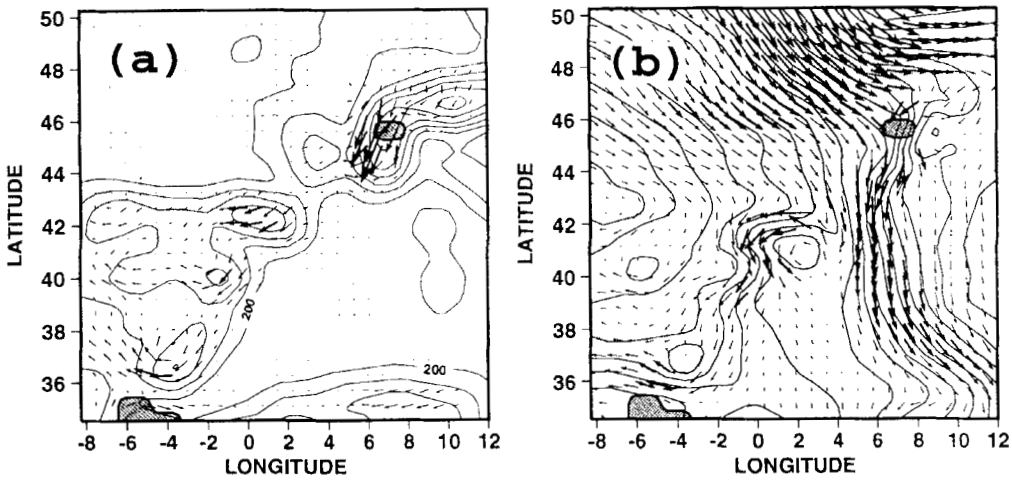


Figure 15. ECMWF 6 h forecast for 06 UTC 15 November 1990. Potential-vorticity fluxes on the isentropic surface $\theta = 293$ K. In the shaded area the isentrope goes below the lowest model level. (a) Orography and potential-vorticity fluxes due to the parametrized frictional forces and diabatic heating, and (b) Bernoulli function (contour interval = 100 J kg$^{-1}$) and total potential-vorticity flux.

in the model than it is in reality, while the lift drag in the model is too small. In other along-ridge configurations, when the temperature gradient across the massif is large, the model pressure drag is close to zero, as is the measured pressure drag, while the Coriolis predictor, which is only relevant in the barotropic context, is not zero. When the incident wind is not purely along the ridge, the model pressure drag is more likely to be related to the ageostrophic response of the model to the mountain forcing. In this case, the model pressure drag is too small, simply because the height of the Pyrénées is too small in the model. In fact a good predictor of the pressure drag, which works for the model pressure drag as well as for the measured drag, is:

$$\rho_0 NV(Z_{MAX} - Z_{MIN})^2/L$$

where $N$ and $V$ are the upstream Brunt–Väisälä frequency and wind perpendicular to the mountain, respectively, $L$ is the transect length along which the drag is measured and $(Z_{MAX} - Z_{MIN})$ is the maximum mountain height in the model. To apply this result to the measured drag (Bessemoulin *et al.* 1993), $(Z_{MAX} - Z_{MIN})$ has to be the mountain height measured on the microbarograph network. Then it is not surprising that the drag in the ECMWF model is a factor of two smaller than the measured pressure drag. It corresponds to the square of the ratio between the mountain height measured on the PYREX transect and the mountain height in the model. In all cases, it was found that the subgrid-scale gravity-wave drag scheme does not make up this deficit, while in some strong wind cases, the boundary-layer drag enhances the total mountain drag to values close to the measured pressure drag. In this discussion, the boundary-layer drag is mainly viewed as a way to increase the mountain drag over the Pyrénées. Sometimes, it compensates for the misrepresentation of the mesoscale mountain, which in reality decelerates the flow at low level more significantly than it does in the model.

Above the mountain summit, a qualitative comparison between the momentum fluxes from the model (i.e. the resolved Reynolds stress together with the parametrized gravity-wave stress and the turbulent stress) and those measured shows that there is no need to enhance any of them at high levels (i.e. significantly above the actual mountain top). On

the other hand, these measurements show that the parametrized drag should be enhanced just above the actual mountain top (between 3 km and 5 km), where aircraft flights observe strong gradients of the momentum fluxes and turbulence. This corresponds to levels which are significantly higher than the model-mountain boundary layer. At these altitudes, no significant drag is exerted in the ECMWF model.

Nevertheless, it appears that all these momentum fluxes above the actual mountain top are small compared with the surface total drag. This means that a description of the low-level dynamics is essential to understand the processes which can explain the drag difference between the ECMWF model and reality. These results were further supported by comparing the ECMWF model performance with a mesoscale analysis done with the Peridot model. Although the Peridot system has its own defects, it seems reasonable to assume that it has a more realistic response than the ECMWF model. Diagnostics on an isentropic surface show that the mesoscale model produces irreversible flow detachment to the lee of the mountain when the isentropes intersect the massif. The ECMWF model underestimates this kind of low-level flow behaviour. On the other hand, the ECMWF model overestimates long lee waves, which sometimes break and lead to neutral layers in the mid-troposphere which are not observed. When these waves are not too large in amplitude and when the low-level dissipation is quite large compared with the pressure drag, the ECMWF model behaves well. It reproduces, via an interaction between the non-conservative parametrized forces and the resolved dynamics, a low-level wake which is realistic.

These results lead to the following conclusion concerning the future developments of the so-called gravity-wave drag schemes. First, the amplitude of the missing drag is related to the fact that the mountain in the model is not high enough. It is clear that this missing drag could be provided by using a higher mountain in the model. As shown in this study this is not suitable, since the model response to the orography often has a strong wave signal, which is not observed, and whose feedback effect on the model dynamics is not well controlled. A higher orography would enhance this kind of failing. This study has also shown that the model behaves quite well when the subgrid-scale drags are large. It means that a parametrization of the missing drag is more reliable than increasing the mountain height. Concerning its vertical distribution, there are three different areas where this drag should act. At high levels (i.e. near the tropopause) it seems that the model, via the gravity-wave drag scheme, already provides enough drag. Around the actual mountain top, aircraft data indicate drags which are absent from the model. Such a drag should be provided in the model, decelerating the flow significantly above the actual orography rather than above the model orography. Between the actual mountain top and the model mountain top, no direct information exists. However, comparison with the Peridot analysis indicates that significant drag should be provided there. This is physically supported by the fact that, in the present version of the model, the low-level dynamics gain realism (as well as numerical consistency) when controlled by large boundary-layer dissipation. This supports the current development of a new subgrid-scale orography scheme at the ECMWF, in which significant drags are delivered to the atmosphere at these levels, to represent the barrier effects of high and narrow mountains.

## Acknowledgements

I would like to thank Dr Philippe Bougeault, who managed PYREX and has provided the measured momentum fluxes used in this paper. I would also like to thank Dr Pierre Bessemoulin, as responsible of the team which measured and calculated the pressure drag during PYREX. I would like to express my gratitude to Dr Graeme Kelly, who made the

ECMWF re-analysis using the PYREX sounding. I have enjoyed helpful discussions on these results with Dr Martin Miller, who also made essential comments on the manuscript. I would also like to thank Dr Anton Beljaars and Pedro Viterbo for the very helpful discussions we had on the representation of subgrid-scale orography in the boundary-layer scheme, and Dr Nicolas Hall who made many corrections to the manuscript.

The PYREX experiment was made possible by the participation of a large number of institutes from France, Spain, and Germany. It was funded by Météo-France, the Instituto National de Meteorologia (Spain), the Institut National des Sciences de l'Univers (ARAT, PAMOS and PAMOY programs), the Centre National d'Etudes Spatiales, Electricité de France, Region Midi-Pyrénées, and the Deutsche Forschungsanstalt für Luft und Raumfahrt. I would like to express my deep appreciation to the many colleagues who have participated in the success of the experiment through enormous personal commitment.

## References

Bessemoulin, P., Bougeault, P., Genoves, A., Jansa Clar, A. and Puech, D. 1993 Mountain pressure drag during PYREX. *Beitr. Phys. Atmos.*, **66,** 305–325

Blondin, C. 1991 Parametrization of land-surface processes in numerical weather prediction. Pp. 31–54 in *Land surface evaporation, measurement and parameterization*. Eds. T. J. Schmugg and J. C. Andre. Springer-Verlag

Boer, G. J., McFarlane, N. A., Laprise, R., Henderson, J. D. and Blanchet, J. P. 1984 The Canadian Climate Centre spectral atmospheric general circulation model. *Atmos.–Ocean*, **22,** 397–429

Bougeault, P. and Mercusot, C. 1992 'Atlas des reanalyses PERIDOT de l'experience PYREX'. Note de travail N°8 du groupe de meteorologie a moyenne echelle. CNRM, F-31057 Toulouse, France.

Bougeault, P., Jansa, A., Attie, J. L., Beau, I., Benech, B., Benoit, B., Bessemoulin, P., Caccia, J. L., Campins, J., Carrissimo, B., Champeaux, J. L., Crochet, M., Druilhet, A., Durand, P., Elkhalfi, A., Flamant, P., Genoves, A., Georgelin, M., Hoinka, K. P., Klaus, V., Koffi, E., Kotroni, V., Mazaudier, C., Pelon, J., Petitdidier, M., Pointin, Y., Puech, D., Richard, E., Satomura, T., Stein, J. and Tannhauser, D. 1993 The atmospheric momentum budget over a major mountain range: first results of the PYREX field program. *Ann. Geophysicae*, **11,** 395–418

Clark, T. L. and Peltier, W. R. 1984 Critical level reflection and the resonant growth of non-linear mountain waves. *J. Atmos. Sci.*, **41,** 3122–3134

Davies, H. C. and Phillips, P. D. 1985 Mountain drag along the Gotthard section during ALPEX. *J. Atmos. Sci.*, **42,** 2093–2109

Grant, A. L. M. and Mason, P. J. 1990 Observation of boundary-layer structure over complex terrain. *Q. J. R. Meteorol. Soc.*, **116,** 159–186

Haynes, P. H. and McIntyre, M. E. 1987 On the evolution of vorticity and potential vorticity in the presence of diabatic heating and frictional or other forces. *J. Atmos. Sci.*, **44,** 828–841

Hoinka, K. P. 1985 Observation of the airflow over the Alps during a foehn event. *Q. J. R. Meteorol. Soc.*, **111,** 199–224

Lott, F. and Teitelbaum, H. 1993 Linear unsteady mountain waves. *Tellus*, **45a,** 201–220

Louis, J. 1979 A parametric model of vertical eddy fluxes in the atmosphere. *Boundary-Layer Meteorol.*, **17,** 187–202

Miller, M. J., Palmer, T. N. and Swinbank, R. 1989 Parametrization and influence of subgridscale orography in general circulation and numerical weather prediction models. *Meteorol. Atmos. Phys.*, **40,** 84–109

| | | |
|---|---|---|
| Monin, A. S. and Obukhov, A. M. | 1954 | Basic regularity in turbulent mixing in the surface layer of the atmosphere. Akad. Nauk. S.S.S.R. trud. *Geofiz. Inst.*, Tr. **24,** 163–187 |
| Miranda, P. M. A. and James, I. N. | 1992 | Non-linear three-dimensional effects on gravity-wave drag: Splitting flow and breaking waves. *Q. J. R. Meteorol. Soc.*, **118,** 1057–1081 |
| Palmer, T. N., Shutts, G. J. and Swinbank, R. | 1986 | Alleviation of systematic westerly bias in general circulation and numerical weather prediction models through an orographic gravity wave drag parametrization. *Q. J. R. Meteorol. Soc.*, **112,** 1001–1039 |
| Peltier, W. R. and Clark, T. L. | 1983 | Nonlinear mountain waves in two and three spatial dimensions. *Q. J. R. Meteorol. Soc.*, **109,** 527–548 |
| Phillips, S. P. | 1984 | Analytical surface pressure and drag for linear hydrostatic flow over three dimensional elliptical mountains. *J. Atmos. Sci.*, **41,** 1073–1084 |
| Pierrehumbert, R. T. and Wyman, B. | 1985 | Upstream effects of mesoscale mountains. *J. Atmos. Sci.*, **42,** 977–1003 |
| Schär, C. | 1993 | A generalization of Bernoulli's theorem. *J. Atmos. Sci.*, **50,** 1437–1443 |
| Schär, C. and Smith, R. B. | 1993 | Shallow water flow past isolated topography. Part I: Vorticity production and wake formation. *J. Atmos. Sci.*, **50,** 1373–1400 |
| Smith, R. B. | 1979a | Some aspects of the quasi-geostrophic flow over mountains. *J. Atmos. Sci.*, **36,** 2385–2393 |
| | 1979b | The influence of the earth rotation on mountain wave drag. *J. Atmos. Sci.*, **36,** 177–180 |
| | 1985 | On severe downslope winds. *J. Atmos. Sci.*, **42,** 2597–2603 |
| Tibaldi, S. and Geleyn, J.-F. | 1981 | 'The production of a new orography, land-sea mask and associated climatological surface fields for operational purposes'. ECMWF Research Department, Technical Memorandum 40 |
| Thorpe, A. J., Volkert, H. and Heimann, D. | 1993 | Potential vorticity of flow along the Alps. *J. Atmos. Sci.*, **50,** 1573–1590 |
| Wallace, J. M., Tibaldi, S. and Simmons, A. | 1983 | Reduction of systematic forecast errors in the ECMWF model through the introduction of an envelope orography. *Q. J. R. Meteorol. Soc.*, **109,** 683–717 |